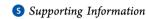


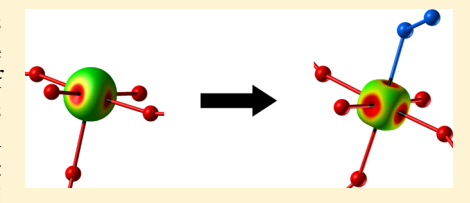
Optimizing Oxygen Reduction Catalyst Morphologies from First **Principles**

Ehsan A. Ahmad,**,†,‡ Vasiliki Tileli,[¶] Denis Kramer,[§] Giuseppe Mallia,†,‡ Kelsey A. Stoerzinger, [∥] Yang Shao-Horn, ^{∥,#} Anthony R. Kucernak,† and Nicholas M. Harrison,†,‡,⊥

¹Daresbury Laboratory, Daresbury, Warrington, WA4 4AD, United Kingdom



ABSTRACT: Catalytic activity of perovskites for oxygen reduction (ORR) was recently correlated with bulk d-electron occupancy of the transition metal. We expand on the resultant model, which successfully reproduces the high activity of LaMnO₃ relative to other perovskites, by addressing catalyst surface morphology as an important aspect of the optimal ORR catalyst. The nature of reaction sites on low index surfaces of orthorhombic (Pnma) LaMnO3 is established from First Principles. The adsorption of O2 is markedly influenced by local geometry and



strong electron correlation. Only one of the six reactions sites that result from experimentally confirmed symmetry-breaking Jahn-Teller distortions is found to bind O2 with an intermediate binding energy while facilitating the formation of superoxide, an important ORR intermediate in alkaline media. As demonstrated here for LaMnO3, rational design of the catalyst morphology to promote specific active sites is a highly effective optimization strategy for advanced functional ORR catalysts.

INTRODUCTION

Perovskites have been studied for their activity toward the oxygen reduction reaction (ORR) since the 1970s. 1-3 Interest in alkaline fuel cells (AFCs) has been renewed in the past decade because of the development of suitable hydroxideexchange membrane materials allowing the alkaline equivalent of the proton exchange membrane fuel cell (PEMFC).⁴ In AFC systems low-cost transition metals (TMs) both are stable and catalyze the ORR well, in contrast to the acidic PEMFC where only expensive noble metal catalysts show suitable activity and stability in spite of decades of research.^{5,6} LaMnO₃ has been identified to be among the most catalytically active perovskites, and recent experiments on a range of perovskites suggest that the high performance is linked to the d⁴ character of the Mn³⁺ ion. This has been attributed to the single Mn eg electron allowing for an interaction with O2 molecules that is neither too strong nor too weak.^{7,8}

The strength of the TM-O2 interaction has a significant effect on the activity of perovskite catalysts for the ORR. Previous analysis of the reaction mechanism has focused on the bulk electronic structure and simple models based on the covalent interaction of metals ions with adsorbed species. These models do not give full consideration to the important role of electron correlation in generating strong Jahn-Teller distortions of the MO₆ octahedra in the active d⁴ (and d⁷) perovskites. This gives rise to a symmetry breaking orbital

ordering of the bulk crystal and, as will be shown below, significant variations in surface reaction sites.

There have been previous studies of the adsorption of oxygen on the surface of LaMnO₃, $^{9-11}$ but the majority of studies has focused on solid oxide fuel cell (SOFC) applications and therefore consider only the highly symmetric, high temperature, cubic phase. For the lower operating temperature of AFCs, it is the orbitally ordered orthorhombic phase that is relevant. 12-14 The schematic in Figure 1 shows that the orthorhombic distortion of the low-temperature phase leads to a set of crystallographically distinct surfaces, which are likely to exhibit different reactivities. The manufacturing procedure and resulting surface terminations have also shown to play a crucial role in determining catalytic activity. 15 We use first-principles calculations, which reproduce the effects of strong electronic correlation, to demonstrate that local Jahn–Teller (J–T) distortions play an important role in determining the interaction of O₂ molecules with LaMnO₃ surfaces. The insight gained is of direct relevance to the design of new catalysts.

Previous studies of O₂ adsorption on orthorhombic (*Pnma*) LaMnO₃ have considered the (010) and (001) surfaces. 10,16,17 The studies focus on a range of adsorption modes and binding sites, again with consideration to the SOFC reaction mechanism. 10,16 Among the likely reaction sites in an AFC

Received: June 8, 2015



Α

[†]Department of Chemistry, [‡]Thomas Young Centre, and [¶]Department of Materials, Imperial College London, South Kensington, London SW7 2AZ, U.K.

[§]Faculty of Engineering and the Environment, University of Southampton, University Road, Southampton SO17 1BJ, U.K.

Electrochemical Energy Lab, Department of Materials Science and Engineering, and *Department of Mechanical Engineering, Massachusetts Institute of Technology, 77 Massachusetts Avenue, Cambridge, Massachusetts 02139, United States

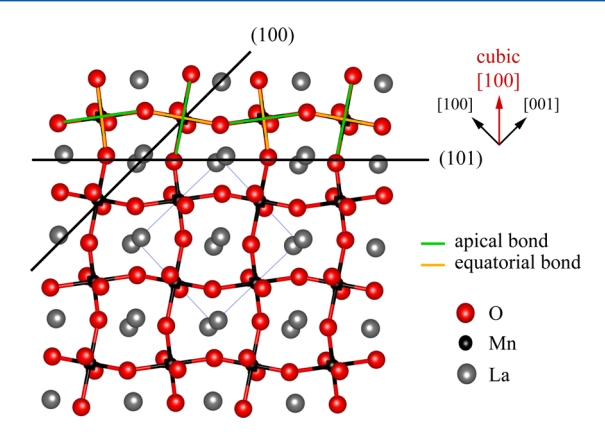


Figure 1. Crystal structure of orthorhombic LaMnO₃; the bulk unit cell is given in blue, and cleavage lines are given in black. Note that the [100] direction of the cubic phase corresponds to [101] in the standard orthorhombic setting (*Pnma*).

environment, only the five-coordinated Mn octaherdon (MnO_5) at the (001) surface has so far been the subject of first-principles investigations.¹⁷

None of the aforementioned studies specify whether the adsorption sites are J–T distorted, while our previous work indicates that a significant local distortion produces Mn–O contacts that are either elongated (apical 2.31 Å) or shortened (equatorial 1.92/1.99 Å) relative to the undistorted octahedra that prevail in the cubic high-temperature phase. As the $\rm O_2$ binding energy is very sensitive to these local distortions, the use of a theory that takes into account strong on-site correlation is essential. This is severely underestimated in studies that use local or semilocal approximations (LDA or GGA) to density functional theory (DFT).

As the nature of O_2 adsorption on the surfaces of orthorhombic LaMnO₃ has yet to be fully explored, we provide a systematic characterization of the binding interaction of O_2 on the full range of sites available on the nonpolar, stoichiometric, and unreconstructed low-index surfaces, established in our previous work. The six distinct types of adsorption site are listed in Table 1 and characterized by the surface on which they

Table 1. TM Adsorption Sites Available in Each Primitive Unit Cell of the Nonpolar, Stoichiometric, and Unreconstructed Low-Index Surfaces of LaMnO₃ (Given in Order of Increasing Surface Formation Energies (E_s))^a

plane	$E_{\rm s}$ relaxed (J/m^2)	Mn sites
(100)	0.98	2 MnO ₅ ^{Ap}
(001)	1.39	$2 \text{ MnO}_{5}^{\text{Eq}}$
(101)	1.36	2 MnO ₅ ^{Ap}
(110)	1.98	$1 \text{ MnO}_5^{\text{Ap}} 1 \text{ MnO}_4^{\text{Ap+Eq}}$

"The sites are J-T distorted octahedra (MnO $_6$) from which O ions have been cleaved (MnO $_5$ or MnO $_4$) in the formation of the surface. The superscripts Ap (apical) and Eq (equatorial) indicate the type of Mn-O bond cleaved from the octahedron to form the site. ¹⁸.

occur, the number of O atoms cleaved to form the site, and the J–T distortion of the Mn–O bond cleaved when forming the site. These sites are indicative of those present in an active catalyst under reaction conditions as they provide examples of apically and equatorially distorted 4- and 5-coordinate Mn sites. The strength of O_2 binding is relatively easily computed and is likely to be an excellent proxy for ORR activity as the formation

of reduced O_2 at the surface is known to be an important intermediate in the high pH environment of the AFC. ^{19–21} The use of binding energies to determine reactivity has been exploited in previous studies where a middle ground is sought between overly strong or weak binding of adsorbates for higher catalytic activity. ^{7,8} We also use the charge transfer to the adsorbed molecule as an indication of the likelihood of reaction steps that depend on the oxidation of the metal site and therefore assert that the combination of binding energy and charge transfer provides a strong indication of the catalytic activity of the sites considered.

RESULTS

To verify the existence of J–T distortion at the orthorhombic $LaMnO_3$ surface, TEM was performed on crystalline powder. A typical image is shown in Figure 2 in which the predicted J–T

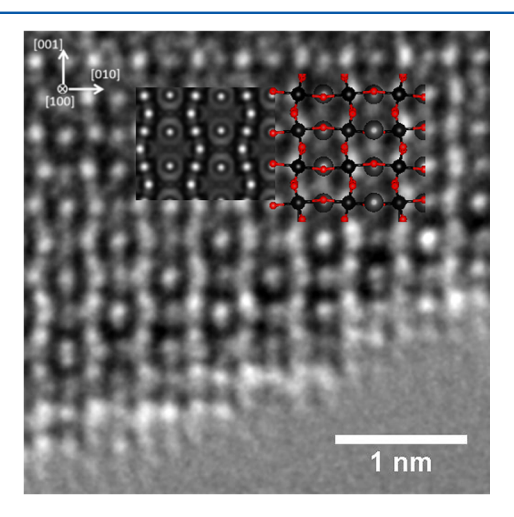


Figure 2. TEM image of a LaMnO₃ particle edge showing the Jahn–Teller distortion at the exposed surface of the (001) plane. In the overlaid schematics, a simulated HRTEM image is shown along with simulations of the atomic positions where La is gray, Mn is black, and O is red.

distortion of Mn-O octahedra in the bulk crystal is clearly visible and is perpetuated from the bulk to the surface. Heuristically, one would be inclined to propose a model for adsorption of O_2 on these distorted surfaces where binding is stronger at lower coordinated Mn sites and at the shorter Mn-O bond provided by equatorial sites relative to the apical sites. While the former is confirmed by our detailed study, the complex nature of the interaction between O_2 and the active sites leads to a nonintuitive dependence of adsorption strength with bond length.

The computed electronic and structural data for the adsorption of O_2 at each site are presented together with binding energies in Table 2. Note that in the DFT calculations of the bulk-like regions of the LaMnO₃ lattice the charge of an O ion estimated by Mulliken population analysis (MPA) is -1.3 lel. Since O^{2-} is the formal oxidation state in bulk LaMnO₃, a value of -0.65 lel for the adsorbed molecule (O_2 q in Table 2) indicates a formal charge of -1 lel. The computed occupations of the surface Mn 3d orbitals are documented in Table 3. These reflect changes in the oxidation state of the surface sites.

It is evident that O₂ adsorption to MnO₅ sites results in strong charge transfer to the molecule and oxidation of Mn

Table 2. Computed Binding Energies (BEs) and Bond Distances (d, in Å) of O_2 Adsorption on the LaMn O_3 Surfaces, Indicating the Initial > Final Adsorption Site Where Different $q(O_2)$ is the Charge Transferred in |e| to O_2 and Resulting Species (Where 0.65 |e| by MPA is Equivalent to One Electron Based on the Bulk Charges)^a

adsorption mode	$d(Mn-O_2)$	d(O-O)	BE (eV)	$q(O_2)$	e_g		
free O ₂	_	1.23	_	0			
(100) MnO ₅ ^{Ap}	2.00	1.31	-0.15	0.48 (O-O ⁻)	1		
$(001) \text{ MnO}_5^{\text{Eq}}$	2.07	1.34	-0.61	0.61 (O-O ⁻)	1		
(101) $MnO_5^{Ap} > La bridge$	-	1.36	-1.17	0.74 (O-O ⁻)	-		
(110) $MnO_5^{Ap} > MnO_4^{Eq-Lateral}$	1.93	1.48	-2.04	1.24 (O-O ²⁻)	2		
(110) $MnO_4^{Ap} > MnO_4^{Eq\text{-End-on}}$	2.03	1.34	-2.32	0.70 (O-O ⁻)	2		
(110) $MnO_4^{Eq} > MnO_4^{Eq-Bidentate}$	1.94	1.46	-2.67	1.04 (O-O ²⁻)	2		
refers to the formal e_g electrons at the active site before O_2 adsorption.							

Table 2 Occumations of the Mr. 2d Orbitale of the

Table 3. Occupations of the Mn 3d Orbitals of the Adsorption Sites Estimated by MPA before and after O_2 Adsorption

adsorption mode	initial 3d (lel)	final 3d (lel)
(100) MnO_5^{Ap}	3.75	3.06
(001) MnO_5^{Eq}	3.75	2.91
(101) $MnO_5^{Ap} > La bridge$	-	-
(110) $MnO_5^{Ap} > MnO_4^{Eq\text{-Lateral}}$	3.69, 4.52	2.70, 3.77
(110) $MnO_4^{Ap} > MnO_4^{Eq-End-on}$	3.69, 4.52	3.21, 3.70
(110) $MnO_4^{Eq} > MnO_4^{Eq-Bidentate}$	3.69, 4.52	3.17, 2.99

from d^4 to d^3 . This is accompanied by a large surface relaxation that may be interpreted as an anti-J-T distortion as the e_g orbital is no longer occupied. This is illustrated very clearly in the spin density at the surface sites before and after O_2 adsorption (Figure 3). The final geometry of each MnO_5 site is therefore rather similar, and the critical role that the apical and equatorial bond lengths of the initial geometry play in the adsorption energetics is not reflected in the final $Mn-O_2$ distances. This results in a rather unexpected trend in adsorption energy with $Mn-O_2$ distance, as typically one would expect stronger binding to be correlated with a shorter interatomic distance.

The differences in the initial coordination of the reaction sites, on the other hand, are reflected in the final $Mn-O_2$ distances. O_2 adsorption on the MnO_4 sites results in significantly lower $d(Mn-O_2)$, as listed in Table 2. The endon adsorption mode on the MnO_4 site proves to be an exception to this, as in this mode the adsorption results in formation of a superoxide (O_2^-) rather than the peroxide (O_2^{2-}) . In the following we analyze the nature of the adsorption at each of the six surface reaction sites (Figures 4–7) in detail.

(100) MnO₅⁶. The lowest binding energy and charge transfer (-0.15 eV and 0.48 lel) are observed for O₂ adsorption on this site. Adsorption takes place at an elongated five-coordinate apical site, and the d(O-O) of 1.31 Å is the least perturbed from that computed for the free O₂ molecule. This is consistent with a general trend that d(O-O) increases in proportion to the binding energy.

(001) MnO $_5^{Eq}$. This site is similar to that on the (100) surface but is formed from the cleavage of an equatorial bond. Adsorption is therefore far stronger with a binding energy of -0.61 eV, with significantly higher charge transfer and, as expected, a somewhat longer d(O-O) of 1.34 Å.

(101) MnO_5^{Ap} > La Bridge. The geometry of the (101) surface results in a unique adsorption mode for the O_2 molecule where it is not bound to the MnO_5^{Ap} site. Instead, as shown in Figure 6, the minimum energy geometry is in a

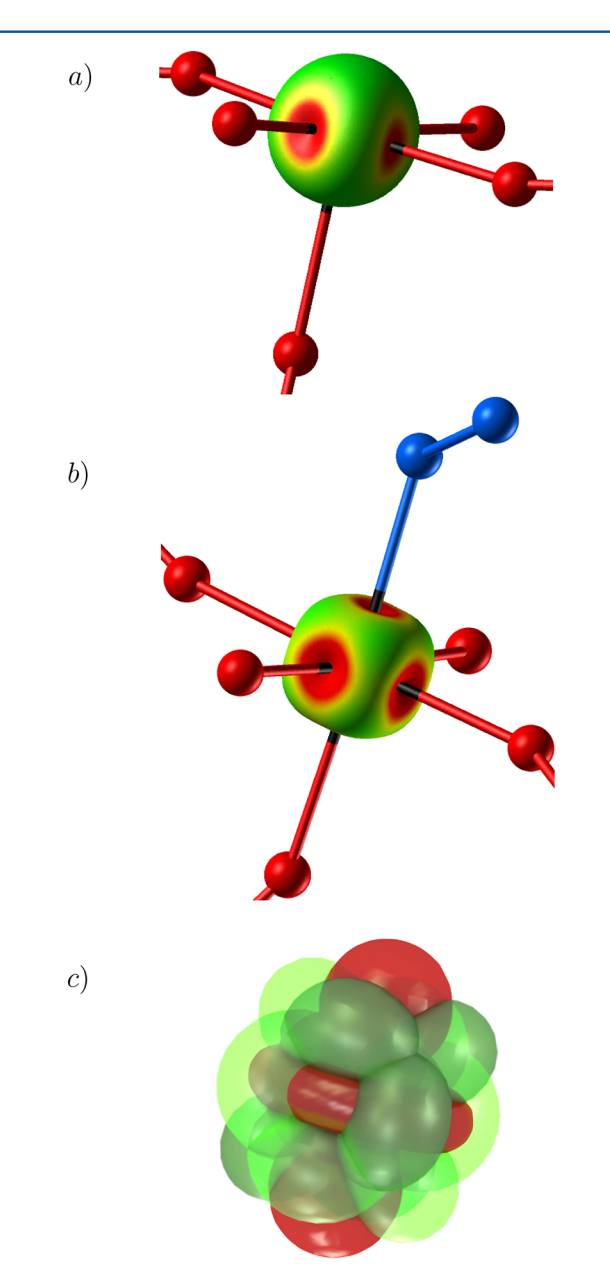


Figure 3. Calculated spin density of (a) the unoccupied Mn_S^{Ap} site on the (100) surface and (b) after O_2 adsorption. (c) Model of the idealized d_{xy} , d_{xz} , d_{yz} , and d_z ² suborbitals for reference.

bridging position between the surface La ions. The binding energy at this site is -1.17 eV compared to the -0.15 we observe for the MnO $_5^{\rm Ap}$ site. The higher binding energy and

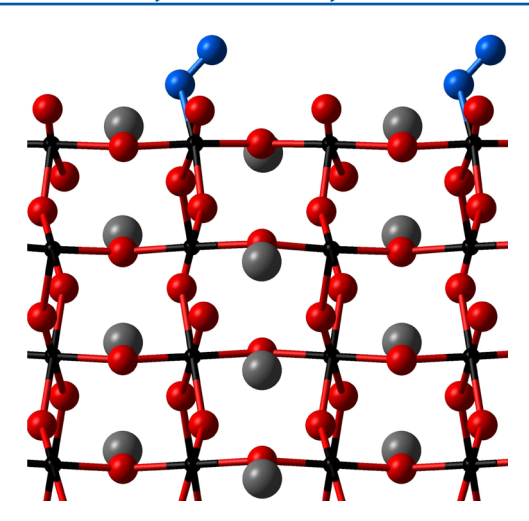


Figure 4. Optimized geometry of the (100) surface with O_2 adsorbed on the $MnO_3^{\rm Ap}$ site.

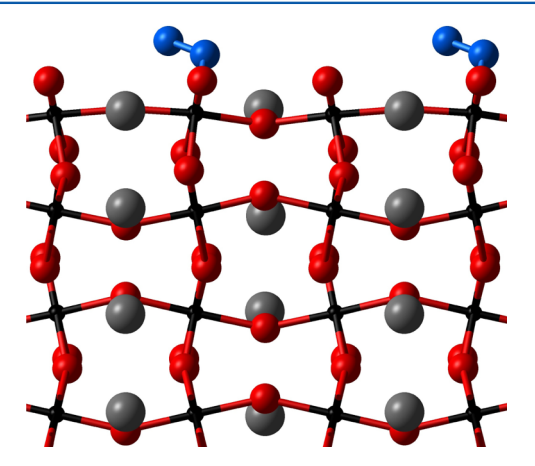


Figure 5. Optimized geometry of the (001) surface with O_2 adsorbed on the MnO_5^{Eq} site.

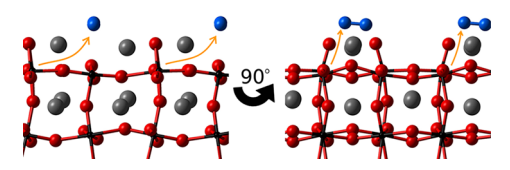


Figure 6. Optimized geometry of the (101) surface with O_2 adsorbed on the La bridge site. Rotated view of the cell is included to clarify O_2 adsorption geometry. Orange arrows indicate charge-donating surface Mn.

charge transfer (-0.74 lel) are reflected in the longer d(O-O) of 1.36 Å. In this case the charge is transferred from fully coordinate MnO_6 octahedra at the surface rather than the surface MnO_5 sites (Figure 6, charge transfer quantified in Supporting Information Table S2). The adsorption geometry and charge transfer here suggest an alternative pathway for the ORR, via electron transfer from the surface rather than from a specific site, which has not been discussed in previous literature. Studies of O_2 adsorption on the La site have only been carried out for the high-temperature cubic LaMn O_3 surfaces, where it is reported that binding is generally weaker than at Mn sites. The (101) surface results in this adsorption mode as access to the Mn site in the second surface layer is sterically inhibited, and the surface layer contains two La ions in close proximity (Figure 6).

(110). This surface presents three distinct types of adsorption sites: MnO_5^{Ap} , MnO_4^{Ap} , and MnO_4^{Eq} . We investigated these sites independently by adsorbing an O_2 molecule at an initial geometry above the sites. However, as observed in Figure 7, three metastable adsorption modes are obtained that center on the MnO_4^{Eq} site: $MnO_4^{Eq-Lateral}$, $MnO_4^{Eq-End-on}$, and

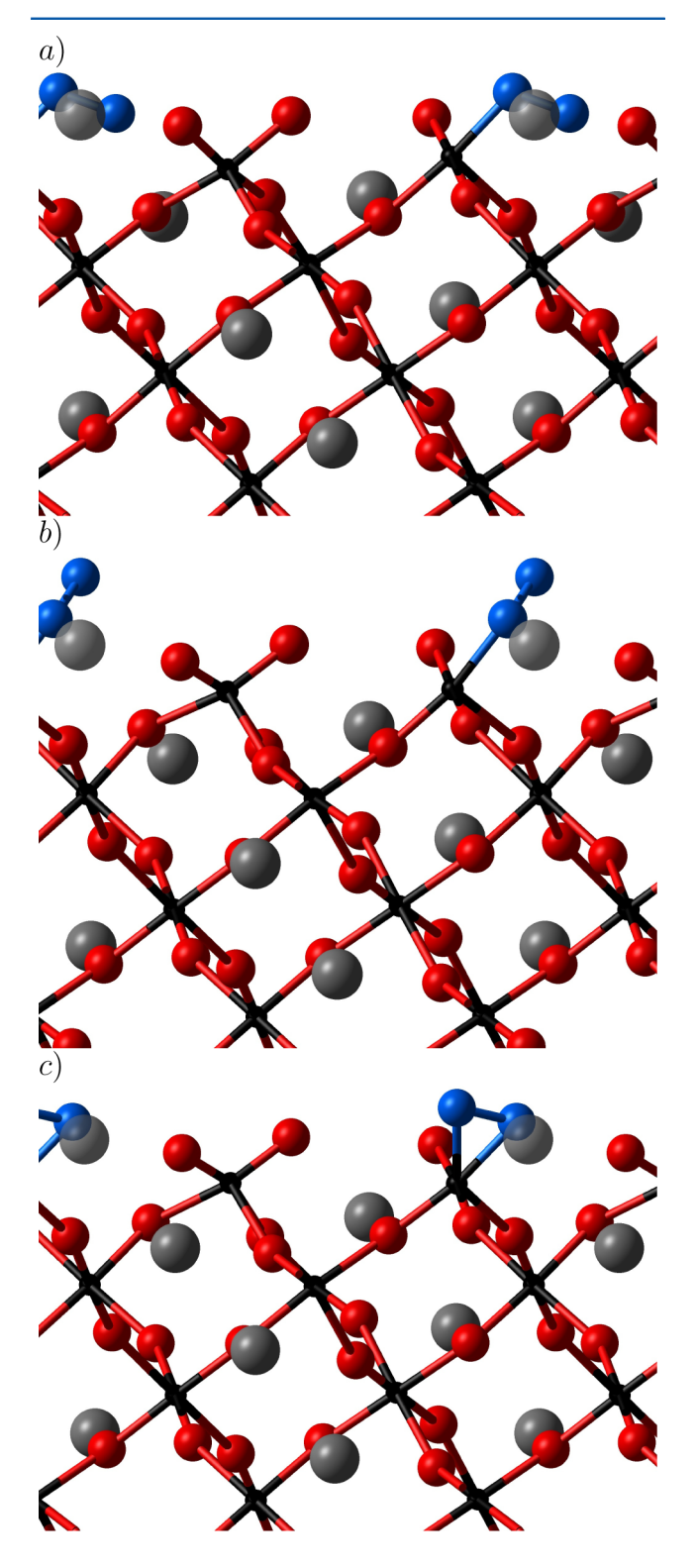


Figure 7. (110) surface showing the adsorption modes: (a) $MnO_4^{\text{Eq-Lateral}}$, (b) $MnO_4^{\text{Eq-End-on}}$, and (c) $MnO_4^{\text{Eq-Bidentate}}$. The corresponding initial adsorption modes are provided in Table 2.

MnO₄^{Eq-Bidentate}, resulting in binding energies of -2.04, -2.32, and -2.67 eV, respectively. The d(O-O), which has been linear with binding energy for the other surfaces, appears to be insensitive to the binding energies on the MnO₄^{Eq} site. The trend in d(O-O) can instead be rationalized more accurately by the variations in charge transfer since increased filling of the antibonding $O_2\pi^*$ orbital destabilizes the O-O bond. The O_2 molecules in the MnO₄^{Eq-Lateral} and MnO₄^{Eq-Bidentate} modes accept -1.24 lel and -1.04 lel, while in the MnO₄^{Eq-End-on} mode it accepts -0.70 lel, resulting in d(O-O) of 1.48, 1.46, and 1.34 Å, respectively.

The differences in binding energy between the adsorption modes on the $MnO_4^{\rm Eq}$ site occur in part due to variations in structural relaxation stemming from the orientation of the O_2 molecule. End-on adsorption is known to be more energetically favorable than lateral adsorption, perhaps due to lower interference with lattice O ions. For the $MnO_4^{\rm Eq-Bidentate}$ mode, the high binding energy can mostly be attributed to the stabilization of both adsorption sites of the MnO_4 octahedron simulataneously, which effectively cancels out its undercoordination and massively stabilizes the surface.

Binding on the MnO_5^{Eq} site of the (110) surface results in shorter $d(Mn-O_2)$ and significantly larger binding energies than observed on the MnO_5^{Eq} of the (001) surface. This can be attributed to undercoordination. The MnO_4^{Eq} site goes from 4 to 5 coordination upon O_2 adsorption but still does not achieve the 6 coordination of the bulk, thus retaining a stronger attraction between the Mn center and the O_2 molecule than observed on a MnO_5^{Eq} site after O_2 adsorption.

DISCUSSION

Our current understanding of optimal ORR activity in d⁴ and d⁷ perovskites is based on the experimental study of a wide range of perovskites.⁷ The data suggest that the requirement for the ORR mechanism to proceed optimally is the existence of a single e_g electron in the TM ion that is able to form a covalent interaction with the adsorbate. As a consequence, variations in the ORR kinetics between manganates (d⁴) and nickelates (d⁷), for instance, are seen to be a result of the changes in TM–O hybridization that modify the covalency of the TM–O₂ (site–adsorbate) bond. However, this simplified concept of a single e_g electron site and a covalent interaction is insufficient to describe the data presented herein. For example, the Mn₅^{Ap} site that shows single e_g occupancy produces weak charge transfer and binding when compared to the doubly e_g occupied MnO₄^{Eq} site, which generates strong charge transfer and binding.

After consideration of the computed binding energies and charge transfer at the various sites, we propose that the ORR mainly proceeds via the disproportionation reaction of adsorbed superoxide O_2^- with water to form the readily desorbed hydroperoxide HOO^- and hydroxide $OH^{-\frac{6,20,21}{2}}$ This pathway only proceeds via the mediation of catalyst sites that lead to the formation of O₂. The sites which result in the formation of strongly bound peroxide O_2^{2-} are likely to give slower OH⁻ formation kinetics due to the increased activation energy required to overcome the stronger Mn-O₂²⁻ bond. Optimal ORR activity is thus determined by two factors: first, the adsorption of O₂ must be neither too weak nor too strong, and second, the charge transfer must result in the formation of superoxide that will react to form hydroperoxide. A typical sample of LaMnO₃ will present a range of surface Mn sites that can form the superoxide species, but due to the strong distortions of the truncated surface octahedra and the variations

in site coordination upon cleavage, only one of these sites is found to be particularly suitable for the ORR: the MnO_5^{Eq} site on the (001) surface. At all other sites the binding energy is either too weak (MnO_5^{Ap} sites) or too strong ($MnO_4^{Ap/Eq}$ sites).

The predicted relative inactivity of many sites on the catalyst may seem to be a strong contraindication for its use in alkaline fuel cells as only 20% of the catalyst surface is predicted to be the (001) surface. This result does, however, suggest a route to optimization of the catalyst through control of the crystallite morphology to maximize the area of the (001) facets. As the data presented make it clear that the binding energy of O_2 is strongly affected by the distortion of the surface MnO_5 sites, we further propose optimization routes that vary the Mn-O distances of the surface sites. This includes doping in nanocrystalline powders or strain engineering in epitaxial thin films. These strategies are highly likely to be successful in catalyst optimization, and their implementation has been shown to be achievable in recent experiments on LaMnO3 thin films. 23

CONCLUSIONS

This work details the structure and energetics of the adsorption sites on the (100), (001), (101), and (110) surfaces of orthorhombic (Pnma) LaMnO₃ by adsorption of molecular oxygen (O₂) in hybrid-exchange (B3LYP) density functional theory calculations. The binding energies of O₂ indicate that MnO₅⁻⁴ adsorption sites formed through cleavage of J–T distorted apical bonds have a weak interaction with O₂, while equatorially cleaved sites bind more strongly. In both instances, O₂ is reduced to superoxide O₂⁻. Lower coordination sites (MnO₄⁻⁵) have overly strong binding and allow for the formation of peroxide O₂²-, which is not likely to be effective for the ORR in alkaline fuel cells (AFCs).

Only the MnO₅^{Eq} site of the (001) surface satisfies the conditions of binding O2 with an energy neither too weak nor too strong and results in the formation of a superoxide species necessary to proceed with the oxygen reduction reaction (ORR) in AFCs. This is shown to be due to the local distortion of the site which is caused by the J-T distortion of bulk MnO₆ octahedra. This model suggests that manipulation of the site activity could be achieved by controlling bulk Mn-O distances through doping and lattice strain. In addition, the total activity can be increased by maximization of the active surface area (surfaces that exhibit MnO₅^{Eq} sites) through control of the crystallite morphology. This work also establishes the need to consider the effects of strong on-site electron correlation in determining the geometry and chemical activity of reaction sites in transition metal oxide catalysts. It is therefore of direct relevance to the discovery and optimization of functional transition metal oxides in many applications.

■ METHODOLOGY

Since previous studies have indicated that the ORR is catalyzed via adsorption at a surface Mn site, 7,20 we adopt an initial geometry for O₂ adsorption with the molecule in an "end-on" orientation at the Mn site at a position reflecting the type of Mn–O bond cleaved when forming the surface (Figure 8). Symmetric adsorption on both sides of a periodic slab is found to converge the adsorption energy rapidly as a function of slab thickness as it prevents the generation of an unphysical electrostatic dipole perpendicular to the surface. The predicted adsorption geometry is then generated by an unconstrained

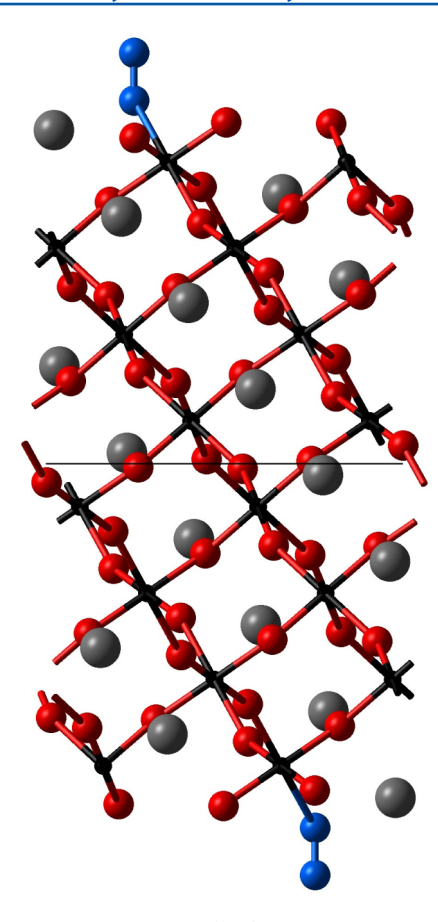


Figure 8. One unit cell of the (110) surface with an O_2 molecule (blue) adsorbed on an apical Mn site (Mn $O_5^{\rm Ap}$), before geometry optimization. The lattice Mn, O, and La are represented by the small black, medium red, and large gray spheres, respectively.

optimization of all atomic coordinates. Details of the surface construction are provided in the Supporting Information.

Binding Energies. In general computed surface binding energies are corrected for basis set superposition error (BSSE) using a counterpoise correction (CPC).^{24–26} For systems studied in this work the CPC method is found to be inapplicable as strong charge rearrangements occur at the adsorption sites during relaxation. The BSSE is therefore estimated at the unrelaxed geometry. The details of this approach and the full list of binding energies obtained using the different methods of estimating BSSE are provided in the Supporting Information.

TEM. The LaMnO $_3$ single-crystal particles were synthesized using a coprecipitation method as described elsewhere. High-resolution transmission electron microscopy (TEM) was performed on a spherical aberration (Cs) corrected at the image plane FEI Titan 80-300 TEM operated at 300 kV. For enhancement of the contrast in the micrographs, the corrector was set at negative spherical aberration imaging conditions, and it was tuned to $-13~\mu m$. Simulations of the atomic positions to assist the interpretation of the high-resolution micrographs were done using the multislice method in JEMS software.

Computational Details. We adopt the hybrid-exchange B3LYP functional for our DFT calculations, as it provides a description of strong on-site correlations and thus an accurate description of the energetics and electronic structure of systems in which strong electron—electron interactions result in electron localization and orbital ordering (particularly for

transition metal oxides). $^{12,29-38}$ It has also recently been shown to provide quantitative agreement between calculated and experimental formation energies for a wide range of Mn-oxides including LaMnO₃. 14

All calculations have been performed using the CRYS-TAL09³⁹ code, based on the expansion of the crystalline orbitals as a linear combination of a local basis set (BS) consisting of atom centered Gaussian orbitals. The Mn and O ions are described by a triple valence all-electron BS: an 86-411d(41) contraction (one s, four sp, and two d shells) and an 8-411d(1) contraction (one s, three sp, and one d shells), respectively; the most diffuse sp(d) exponents are $\alpha^{\rm Mn}=0.4986(0.249)$ and $\alpha^{\rm O}=0.1843(0.6)$ Bohr^{-2,40} The La basis set includes a pseudopotential to describe the core electrons, while the valence part consists of a 411p(411)d(311) contraction scheme (with three s, three p, and three d shells); the most diffuse exponent is $\alpha^{\rm La}=0.15$ Bohr⁻² for each s, p, and d.¹²

The internal coordinates of the slab have been determined by minimization of the total energy within an iterative procedure based on the total energy gradient calculated with respect to the nuclear coordinates. Convergence was determined from the root-mean-square (rms) and the absolute value of the largest component of the forces. The thresholds for the maximum and the rms forces (the maximum and the rms atomic displacements) have been set to 0.00045 and 0.00030 (0.00180 and 0.0012) in atomic units. Geometry optimization was halted when all four conditions were satisfied simultaneously.

ASSOCIATED CONTENT

S Supporting Information

Procedure for calculations and the full Mn 3d orbital occupations of surface Mn ions. The Supporting Information is available free of charge on the ACS Publications website at DOI: 10.1021/acs.jpcc.5b05460.

AUTHOR INFORMATION

Corresponding Author

*E-mail: ea808@imperial.ac.uk.

Notes

The authors declare no competing financial interest.

ACKNOWLEDGMENTS

The authors thank Prof. Jin Suntivich for useful discussions. This work made use of the high performance computing facilities of Imperial College London and—via membership of the UK's HPC Materials Chemistry Consortium funded by EPSRC (EP/F067496)—of HECTOR, the UK's national high-performance computing service, which is provided by UoE HPCx Ltd at the University of Edinburgh, Cray Inc., and NAG Ltd. and funded by the Office of Science and Technology through EPSRC's High End Computing Programme.

■ REFERENCES

- (1) Tseung, A.; Bevan, H. A reversible oxygen electrode. J. Electroanal. Chem. Interfacial Electrochem. 1973, 45, 429–438.
- (2) Matumoto, Y.; Yoneyama, H.; Tamura, H. A new catalyst for cathodic reduction of oxygen: Lanthanum Nickel Oxide. *Chem. Lett.* 1975, 4, 661–662.
- (3) Matsumoto, Y.; Yoneyama, H.; Tamura, H. Catalytic activity for electrochemical reduction of oxygen of lanthanum nickel oxide and related oxides. *J. Electroanal. Chem. Interfacial Electrochem.* **1977**, 79, 319–326.

- (4) Varcoe, J. R.; Atanassov, P.; Dekel, D. R.; Herring, A. M.; Hickner, M. A.; Kohl, P. A.; Kucernak, A. R.; Mustain, W. E.; Nijmeijer, K.; Scott, K.; et al. Anion-exchange membranes in electrochemical energy systems. *Energy Environ. Sci.* **2014**, *7*, 3135–3191.
- (5) Hayashi, M.; Uemura, H.; Shimanoe, K.; Miura, N.; Yamazoe, N. Reverse Micelle Assisted Dispersion of Lanthanum Manganite on Carbon Support for Oxygen Reduction Cathode. *J. Electrochem. Soc.* **2004**, *151*, A158–A163.
- (6) Bidault, F.; Brett, D.; Middleton, P.; Brandon, N. Review of gas diffusion cathodes for alkaline fuel cells. *J. Power Sources* **2009**, *187*, 39–48.
- (7) Suntivich, J.; Gasteiger, H. A.; Yabuuchi, N.; Nakanishi, H.; Goodenough, J. B.; Shao-Horn, Y. Design principles for oxygen-reduction activity on perovskite oxide catalysts for fuel cells and metal air batteries. *Nat. Chem.* **2011**, *3*, 546–550.
- (8) Vojvodic, A.; Norskov, J. K. Optimizing Perovskites for the Water-Splitting Reaction. *Science* **2011**, *334*, 1355–1356.
- (9) Choi, Y.; Mebane, D. S.; Lin, M. C.; Liu, M. Oxygen Reduction on LaMnO₃-Based Cathode Materials in Solid Oxide Fuel Cells. *Chem. Mater.* **2007**, *19*, 1690–1699.
- (10) Kotomin, E. A.; Mastrikov, Y.; Heifets, E.; Maier, J. Adsorption of atomic and molecular oxygen on the LaMnO₃(001) surface: ab initio supercell calculations and thermodynamics. *Phys. Chem. Chem. Phys.* **2008**, *10*, 4644–4649.
- (11) Choi, Y.; Lynch, M. E.; Lin, M. C.; Liu, M. Prediction of O2 Dissociation Kinetics on LaMnO₃-Based Cathode Materials for Solid Oxide Fuel Cells. *J. Phys. Chem. C* **2009**, *113*, 7290–7297.
- (12) Muñoz, D.; Harrison, N. M.; Illas, F. Electronic and magnetic structure of *LaMnO*₃ from hybrid periodic density-functional theory. *Phys. Rev. B: Condens. Matter Mater. Phys.* **2004**, *69*, 085115.
- (13) Goodenough, J. B.; Zhou, J.-S. Orbital ordering in orthorhombic perovskites. *J. Mater. Chem.* **2007**, *17*, 2394–2405.
- (14) Ahmad, E. A.; Liborio, L.; Kramer, D.; Mallia, G.; Kucernak, A. R.; Harrison, N. M. Thermodynamic stability of LaMnO₃ and its competing oxides: A hybrid density functional study of an alkaline fuel cell catalyst. *Phys. Rev. B: Condens. Matter Mater. Phys.* **2011**, 84, 085137
- (15) Symianakis, E.; Malko, D.; Ahmad, E.; Mamede, A.-S.; Paul, J.-F.; Harrison, N.; Kucernak, A. Electrochemical Characterization and Quantified Surface Termination Obtained by Low Energy Ion Scattering and X-ray Photoelectron Spectroscopy of Orthorhombic and Rhombohedral LaMnO₃ Powders. *J. Phys. Chem. C* **2015**, *119*, 12209–12217.
- (16) Mastrikov, Y. A.; Merkle, R.; Heifets, E.; Kotomin, E. A.; Maier, J. Pathways for Oxygen Incorporation in Mixed Conducting Perovskites: A DFT-Based Mechanistic Analysis for (La, Sr)MnO_{3-δ}. *J. Phys. Chem. C* **2010**, *114*, 3017–3027.
- (17) Wang, Y.; Cheng, H.-P. Oxygen Reduction Activity on Perovskite Oxide Surfaces: A Comparative First-Principles Study of LaMnO₃, LaFeO₃, and LaCrO₃. *J. Phys. Chem. C* **2013**, *117*, 2106–2112.
- (18) Ahmad, E. A.; Mallia, G.; Kramer, D.; Kucernak, A. R.; Harrison, N. M. The stability of LaMnO₃ surfaces: a hybrid exchange density functional theory study of an alkaline fuel cell catalyst. *J. Mater. Chem. A* **2013**, *1*, 11152–11162.
- (19) Bielski, B. H.; Cabelli, D. E.; Arudi, R. L.; Ross, A. B. Reactivity of HO_2/O_2^- radicals in aqueous solution. *J. Phys. Chem. Ref. Data* **1985**, *14*, 1041–1100.
- (20) Lima, F. H.; Calegaro, M. L.; Ticianelli, E. A. Investigations of the catalytic properties of manganese oxides for the oxygen reduction reaction in alkaline media. *J. Electroanal. Chem.* **2006**, 590, 152–160.
- (21) Yeager, E. Electrocatalysts for O_2 reduction. *Electrochim. Acta* 1984, 29, 1527–1537.
- (22) Outka, D. A.; Stöhr, J.; Jark, W.; Stevens, P.; Solomon, J.; Madix, R. J. Orientation and bond length of molecular oxygen on Ag(110) and Pt(111): A near-edge x-ray-absorption fine-structure study. *Phys. Rev. B: Condens. Matter Mater. Phys.* 1987, 35, 4119–4122.

- (23) Stoerzinger, K. A.; Risch, M.; Suntivich, J.; Lu, W. M.; Zhou, J.; Biegalski, M. D.; Christen, H. M. Ariando,; Venkatesan, T.; Shao-Horn, Y. Oxygen electrocatalysis on (001)-oriented manganese perovskite films: Mn valency and charge transfer at the nanoscale. *Energy Environ. Sci.* **2013**, *6*, 1582–1588.
- (24) Scaranto, J.; Mallia, G.; Harrison, N. An efficient method for computing the binding energy of an adsorbed molecule within a periodic approach. The application to vinyl fluoride at rutile TiO₂(110) surface. *Comput. Mater. Sci.* **2011**, *50*, 2080–2086.
- (25) Jensen, F. Introduction to Computational Chemsitry; Wiley: New York, 2007.
- (26) Cramer, C. J. Essentials of Computational Chemistry: Theories and Models; Wiley: New York, 2004.
- (27) Jia, C.-L.; Lentzen, M.; Urban, K. High-Resolution Transmission Electron Microscopy Using Negative Spherical Aberration. *Microsc. Microanal.* **2004**, *10*, 174–184.
- (28) Stadelmann, P. A. EMS a software package for electron diffraction analysis and HREM image simulation in materials science. *Ultramicroscopy* **1987**, *21*, 131–145.
- (29) Muscat, J.; Wander, A.; Harrison, N. On the prediction of band gaps from hybrid functional theory. *Chem. Phys. Lett.* **2001**, 342, 397–401
- (30) Mallia, G.; Harrison, N. M. Magnetic moment and coupling mechanism of iron-doped rutile *TiO2* from first principles. *Phys. Rev. B: Condens. Matter Mater. Phys.* **2007**, 75, 165201.
- (31) Wilson, N. C.; Russo, S. P.; Muscat, J.; Harrison, N. M. Highpressure phases of FeTiO₃ from first principles. *Phys. Rev. B: Condens. Matter Mater. Phys.* **2005**, 72, 024110.
- (32) Cora, F.; Alfredsson, M.; Mallia, G.; Middlemiss, D. S.; Mackrodt, W. C.; Dovesi, R.; Orlando, R. In *Principles and Applications of Density Functional Theory in Inorganic Chemistry II*; Kaltsoyannis, N., McGrady, J., Eds.; Structure & Bonding; Springer Berlin/Heidelberg: Berlin, 2004; Vol. 113, pp 171–232.
- (33) De Fusco, G. C.; Montanari, B.; Harrison, N. M. Half-metallicity in the ferrimagnet *Nb* (*TCNE*) 2 from first principles. *Phys. Rev. B: Condens. Matter Mater. Phys.* **2010**, 82, 220404.
- (34) Ge, L.; Jefferson, J. H.; Montanari, B.; Harrison, N. M.; Pettifor, D. G.; Briggs, G. A. D. Effects of Doping on Electronic Structure and Correlations in Carbon Peapods. *ACS Nano* **2009**, *3*, 1069–1076.
- (35) De Fusco, G. C.; Pisani, L.; Montanari, B.; Harrison, N. M. Density functional study of the magnetic coupling in V(TCNE)₂. *Phys. Rev. B: Condens. Matter Mater. Phys.* **2009**, 79, 085201.
- (36) Liborio, L.; Mallia, G.; Harrison, N. Electronic structure of the Ti₄O₇ Magnéli phase. *Phys. Rev. B: Condens. Matter Mater. Phys.* **2009**, 79, 245133.
- (37) Bailey, C. L.; Liborio, L.; Mallia, G.; Tomić, S.; Harrison, N. M. Defect physics of CuGaS₂. *Phys. Rev. B: Condens. Matter Mater. Phys.* **2010**, *81*, 205214.
- (38) Liborio, L. M.; Bailey, C. L.; Mallia, G.; Tomic, S.; Harrison, N. M. Chemistry of defect induced photoluminescence in chalcopyrites: The case of CuAlS₂. *J. Appl. Phys.* **2011**, *109*, 023519.
- (39) Dovesi, R.; Saunders, V. R.; Roetti, C.; Orlando, R.; Zicovich-Wilson, C. M.; Pascale, F.; Civalleri, B.; Doll, K.; Harrison, N.; Bush, I. J. et al. *CRYSTAL09 User's Manual*; Università di Torino: Torino, 2010.
- (40) http://www.crystal.unito.it/Basis_Sets/Ptable.html (accessed September 1, 2014).